Climate Dynamics (1999) 15:63–80

A. Vintzileos · P. Delecluse · R. Sadourny

On the mechanisms in a tropical ocean–global atmosphere coupled general circulation model. Part II: interannual variability and its relation to the seasonal cycle

Received: 7 April 1997 / Accepted: 15 July 1998

Abstract The thirty year simulation of the coupled global atmosphere-tropical Pacific Ocean general circulation model of the Laboratoire de Météorologie Dynamique and the Laboratoire d'Océanographie Dynamique et de Climatologie presented in Part I is further investigated in order to understand the mechanisms of interannual variability. The model does simulate interannual events with ENSO characteristics; the dominant periodicity is quasi-biennial, though strong events are separated by four year intervals. The mechanism that is responsible for seasonal oscillations, identified in Part I, is also active in interannual variability with the difference that now the Western Pacific is dynamically involved. A warm interannual phase is associated with an equatorward shift of the ITCZ in the Western and Central Pacific. The coupling between the ITCZ and the ocean circulation is then responsible for the cooling of the equatorial subsurface by the draining mechanism. Cold subsurface temperature anomalies then propagate eastward along the mean equatorial thermocline. Upon reaching the Eastern Pacific where the mean thermocline is shallow, cold subsurface anomalies affect surface temperatures and reverse the phase of the oscillation. The preferred season for efficient eastward propagation of thermocline depth temperature anomalies is boreal autumn, when draining of equatorial waters towards higher latitudes is weaker than in spring by a factor of six. In that way, the annual cycle acts as a dam that synchronizes lower frequency oscillations.

A. Vintzileos (✉)
Laboratoire de Météorologie Dynamique du CNRS,
Université Pierre et Marie Curie, Tour 25, Boite 99,
4, Place Jussieu, 75252 Paris Cedex 05, France
E-mail: augustin@lmd.jussieu.fz

P. Delecluse
Laboratoire d'Océanographie Dynamique et de Climatologie,
UMR: CNRS/ORSTOM/Université Pierre et Marie Curie,
Tour 26, étage 4, 4, Place Jussieu, 75252 Paris Cedex 05, France

R. Sadourny
Laboratoire de Météorologie Dynamique du CNRS,
Ecole Normale Supérieure, 24, rue Lhomond, 75231
Paris Cedex 05, France

1 Introduction

The most important component of climate variability after the seasonal cycle is the El Niño – Southern Oscillation (ENSO). Although this phenomenon concerns the quasi-totality of climate fields on a global scale through teleconnections, its center of action is located in the tropical Pacific. As noted by Bjerknes (1969), ENSO is a manifestation of the coupling between the ocean and the atmosphere in the equatorial Pacific, mainly between the zonal SST gradient along the equator and the intensity of the Walker circulation. The Bjerknes hypothesis can explain the evolution towards warm or cold conditions: weak trades are responsible for a decrease of the zonal SST gradient which further decreases the trades. Nevertheless, this positive feedback loop alone cannot explain the oscillatory nature of ENSO.

Additional mechanisms responsible for phase inversions have been actively searched using simplified coupled models of the tropical Pacific system (e.g., Lau 1980; Philander et al. 1984; Hirst 1986; Zebiak and Cane 1987; Neelin 1991). Two principal mechanisms were proposed in the late 1980s: the delayed oscillator (Suarez and Schopf 1988; Battisti and Hirst 1989), and unstable U-modes or SST-modes (Hirst 1986; Neelin 1991). According to the delayed oscillator hypothesis, the ocean equatorial subsurface state is not in equilibrium with the local atmospheric forcing. Kelvin waves, forced by the reflection of Rossby waves at the western boundary, carry information opposite in sign to the original anomalous oceanic equatorial signal. In the Eastern Pacific where the mean thermocline is shallow,

subsurface anomalies affect surface temperatures and eventually reverse the phase or surface conditions. An important factor for the periodicity of oscillations is the length of the ocean basin. On the other hand, as shown by Hirst (1986), in the coupling process, Kelvin and Rossby waves are damped, while an unstable mode (U-mode) appears with a periodicity comparable to ENSO time scales. Further, Neelin (1991) considers that the propagation of Kelvin or Rossby waves is too fast to explain interannual variability (fast wave limit). Again, an unstable mode (SST-mode) associated with the prognostic SST equation is responsible for interannual behavior. Unstable modes can be explained by a lag between the atmospheric forcing and the evolution of the SST. In a series of three papers Jin and Neelin (1993a, b), and Neelin and Jin (1993) describe a SST-ocean mode which contains SST modes and the delayed oscillator mechanism as limits. An alternative hypothesis proposed by Wyrtki (1985) explains the ENSO cycle as a discharge of energy accumulated in the equatorial neighborhood; a discharge that leads to cold conditions. According to Wyrtki's hypothesis, the time scale of ENSO is set by the slow build-up of heat content in the Western Pacific; when some threshold is reached, the system collapses under the influence of high-frequency atmospheric variability. Jin (1996, 1997) describes a conceptual model for interannual oscillations based on the hypothesis of Bjerknes (1969), Wyrtki (1985) and Cane and Zebiak (1985). According to his interpretation, the build-up of heat content in the Western Pacific depends on the fluctuation of the SST in the Eastern Pacific which controls the Walker circulation; in parallel, heat content fluctuations in the Western Pacific are responsible for changes in the Eastern Pacific heat content and thus for changes in the SST there, allowing for phase transitions.

Despite their success in proposing mechanisms for phase inversion, simplified models are not able to represent, at least in an interactive way, important features of the tropical climate such as the Inter Tropical Convergence Zone (ITCZ). The inclusion of such features demands the use of coupled general circulation models of the atmosphere and the ocean. In this respect, two modelling approaches have been extensively used: coupled models of the global atmosphere and ocean (G-CGCMs), and coupled models of the global atmosphere and the tropical Pacific ocean (TOGA-CGCMs). The advantage of using the latter approach is that, for given computing limitations, the resolution of the ocean model can be increased in the core region of ENSO. Studies on the impact of discretization (Philander et al. 1992; Lau et al. 1992) suggest that, although these two categories of models do simulate ENSO behavior, their physics are different: in their tropical model, subsurface dynamics set the memory for phase inversions while in the global model, interannual cyclicity depends on lags between the atmospheric forcing and the ocean surface layer response. Analysis of observations (Zhang and Levitus 1996) indicates that subsurface dynamics is important for interannual oscillations thus suggesting that TOGA-CGCM physics is closer to reality.

As noted by Rasmusson and Carpenter (1983), the evolution of a typical interannual event can be described by means of calendar months thus indicating a synchronization with the seasonal cycle. Among other factors, a key to unstable evolution is the Inter Tropical Convergence Zone (ITCZ) nearing to the equator (Hirst 1986). Therefore, a possible candidate for the phase locking of the interannual variability is the seasonal oscillation of the ITCZ which in the Eastern Pacific reaches its southernmost position in spring (Waliser and Gautier 1993). However, an alternative hypothesis exists which proposes late summer as the most sensitive period, due to increased zonal SST gradient (e.g. Cane and Zebiak 1987).

In Part I of this study (Vintzileos et al. 1997), we demonstrated the crucial role of the ITCZ-ocean interaction for the tropical Pacific annual cycle. The atmospheric motion between the equator and 10 °N is characterized by a meridional dipole of anticyclonic/cyclonic vorticity with the ITCZ in between. The intensity of this dipole depends on meridional SST gradients, on the CISK mechanism, and on the lower branch of the Walker circulation which in turn is in equilibrium with the zonal SST gradients. Due to surface friction, a dipole of Ekman subsidence/ascendance is simultaneously formed. In part I we demonstrated that to a great extent, atmospheric Ekman subsidence, averaged between 2 °N–4 °N, controls oceanic downwelling at a depth of 70 m. In turn, this downwelling oceanic branch recycles a portion of equatorially upwelled waters, thus feeding equatorial subsurface convergence, the rest of the water being *drained* out to the north of 5 °N. Strong draining during boreal spring is accompanied by reduced meridional gradients of SST, an ITCZ close to the equator, cold equatorial subsurface temperature fluctuations that propagate eastwards, and a decrease in the intensity of both the North Equatorial Counter Current (NECC, eastward) and the northern branch of the South Equatorial Current (SEC, westward). After some time lag due to eastward propagation along the thermocline, the cold subsurface anomalies affect surface conditions in the east, thus premitting the transition from warm surface conditions to cold ones. The annual cycle is confined to the Central and Eastern Pacific. However, it can be disturbed by surface temperature anomalies arriving from the Western Pacific. Consider for example cold subsurface temperature anomalies propagating eastward into the Central Pacific during boreal autumn: the subsurface warming normal at this time of the year will be weakened, and so will the next surface warming six months later. If the Western Pacific is dynamically active, departures from the mean seasonal behavior might exist.

This study attempts to isolate some characteristics of the simulated interannual variability, allowing us to define an "average" ENSO behavior. The work is structured as follows. In Sect. 2 we establish the dominant ENSO nature of the simulated interannual variability and the relevance of draining for interannual subsurface temperature fluctuations in the Western Pacific. The coupled evolution of key fields in terms of calendar months is described in Sect. 3. In Sect. 4, we further investigate the quasi-biennial mode and we examine the impact of mean seasonal draining on the timing of interannual variability. We then summarize and conclude in Sect. 5. For a description of the individual components of the coupled model and of the interface, the reader is referred to Part I of this study.

2 Simulated interannual behavior

The evolution of sea surface temperature anomalies, defined as departures from the mean seasonal cycle (computed from the 29 last years of the integration), in a meridionally reduced Niño 3 box (2 °S–2 °N; 150 °W–90 °W) is presented in Fig. 1; to help identify strong events (in model sense), we have added levels corresponding to ± 1.96 times the standard deviation. The first strong event is a cold one with an amplitude reaching -1 °C; it is followed by two slightly weaker but still significant cold events. Then, two strong warm events occur, separated by 4.8 years. A fourth cold event is then followed by a persistent 4-y moderately warm phase. Finally, we notice two strong warm events separated by a 3.8 y interval. The first and third warm events have a lifetime of approximately one year while the second continues for roughly 20 months. Rapid inspection of Fig. 1 indicates a dominant periodicity in the order of two years, though the strongest events are separated by periods of roughly four years. It must be noted that the simulated interannual variability is weaker than observations by a factor of two, as was already the case for the seasonal cycle.

An empirical orthogonal function (EOF) analysis of the SST over the last 29 y of integration has been used to extract the dominant signature of interannual variability. Data from the 30 °S–30 °N band are used. The time evolution of the dominant variability mode, explaining 28% of the variance, is plotted in Fig. 2a against an idealized seasonal cycle peaking in April with an amplitude equal to 1.96 times the standard deviation. The correlation between the Niño 3 time series of Fig. 1 and the principal component of Fig. 2a is as high as 92%; it is maximized for a zero time lag. The spatial structure of this first EOF is shown in Fig. 2b. With respect to observations, its biases are similar to those of the average cold tongue already noticed in Part I: mainly, it is too narrow and penetrates too much into the West Pacific. There are five simulated episodes that can be considered as strong (amplitude stronger than 1.96 times the standard deviation) from the viewpoint of EOF 1; their respective peaks occur in months 39, 62, 76, 134 and 303, i.e. during late winter or early spring. At the end of the simulation (December), sixth strong warm episode is developing.

The atmospheric counterpart of this first SST variability mode (El Niño) is illustrated in Fig. 3 by the correlation of the first SST principal component with the time evolution of sea level pressure (SLP) anomalies at each grid point; here the SLP anomaly field has been filtered using a 9-month running average. The correlation structure is a dipole with centers over the East Pacific and the Indonesian region. As expected, a warm SST event is associated with low pressure anomalies over the Eastern Pacific and high-pressure anomalies over the Indian ocean and the Western Pacific. This Southern Oscillation dipole forms with the El Niño variability the simulated ENSO phenomenon. The general structure of the SO dipole is close to observations (Trenberth and Shea 1987), though the high-pressure extension into the Indian Ocean appears too strong.

The link from surface pressure to SST anomalies is established by an EOF analysis of the wind stresses, restricted to the 10 °S–10 °N longitudinal band to filter out the strong higher latitude variability. Figure 4a shows the third variability mode (8% of total variance) of the zonal wind stress, and Fig. 4b the first variability mode (13% of total variance) of the meridional wind stress. These two EOFs have been selected because their time coefficients show the highest correlations with those of the first SST EOF mode: 0.55 for the meridional stress and 0.61 for the zonal stress (simultaneous correlations are the strongest: lagged correlations drop under 0.25). For the zonal wind stress, the first and second EOFs explain 13% and 10% of the total variance respectively; their time series (not shown) show high frequency behavior with a rather white spectrum. During a warm event, positive zonal wind stress anomalies are located over the equatorial Pacific with a preference for Central and Western sectors, while, to the north of 3 °N, negative anomalies centered at 170 °E and 7 °N dominate. Also during a warm event, the meridional wind stress shows negative anomalies in the Northern hemisphere and positive anomalies south of 2 °S–4 °S. The implication of both structures for the divergence and vorticity fields are consistent with an equatorward shift of organized convection. The meridional oscillation of the ITCZ associated to warm and cold events is indeed confirmed by Fig. 4c, which shows the correlation of the precipitation anomaly (filtered by a 9-month running mean) with the first SST principal component. An immediate consequence is weaker (stronger) than normal subsidence between the equator and the average ITCZ latitude during warm (cold) events. Therefore, warm events are associated with increased meridional draining of surface waters in the Western and Central Pacific.

Along a Central Pacific section (150 °W), between 2 °N and 4 °N, seasonal subsurface temperature fluctuations lag wind stress curl

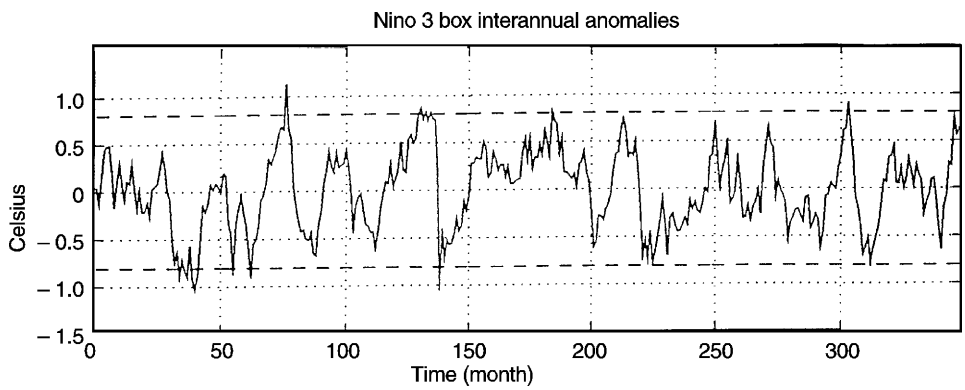

Fig. 1 Time series of interannual monthly mean SST anomalies (*continuous line*) in a meridionally restricted Niño 3 box (2 °S–2 °N, 150 °W–90 °W). The *dashed lines* correspond to ± 1.96 times the standard deviation identifying strong events

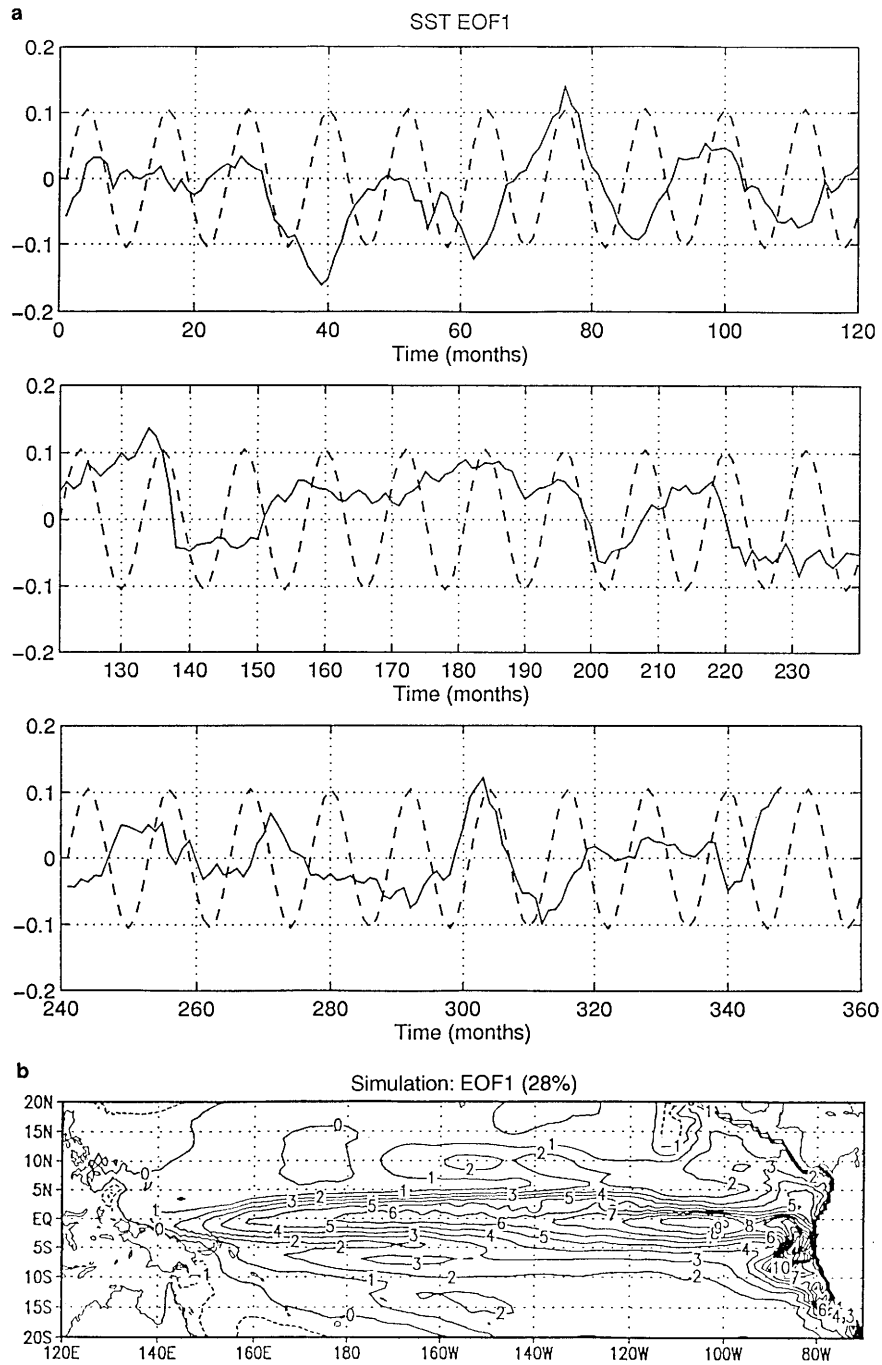

Fig. 2a Three panel time series of the first interannual EOF of the simulated SST (*continuous line*) explaining 28% of total variance, superimposed on an idealized seasonal cycle (*dashed line*) with maximum values in April and an amplitude corresponding to 1.96 times the standard deviation. **b** The spatial structure of the simulated SST first EOF

fluctuations by two to three months (see Part I). We check whether the same behavior exists in the Western Pacific (160 °E) by correlating subsurface temperature averaged between 3 °S and 3 °N and between 70 and 210 m with the difference between the wind stress curl in the Northern Hemisphere (2 °N–4 °N average) and the wind stress curl in the Southern Hemisphere (4 °S–2 °S average), a measure of Ekman pumping involving both hemispheres as required for the Western Pacific. Both quantities are filtered by a 1.8–4 y band-pass filter (Murakami 1979). The correlation between the resulting time series is maximized (-86%) when the wind stress curl leads the subsurface temperature by two months. Figure 5 shows the relation between the wind stress curl at time t and the subsurface temperature at time $t + 2$ months. We further investigate the effects of draining on interannual subsurface temperature fluctuations in the Western Pacific by considering filtered meridional and vertical transports, and temperature fluctuations two months later in a meridional section at 160 °W. Conditions during a warm surface phase (e.g. during month 77—May) and a cold surface phase (e.g. during month 147—March) are contrasted in Fig. 6. During a cold surface phase, equatorially upwelled water is almost entirely recycled feeding equatorial subsurface convergence; water plunges at 3 °S and 3 °N reaching depths of 180 m. As a result, subsurface temperatures increase. In contrast, during warm surface conditions draining is strong, especially in the Northern Hemisphere where most of the equatorially upwelled water flows to the north of 5 °N.

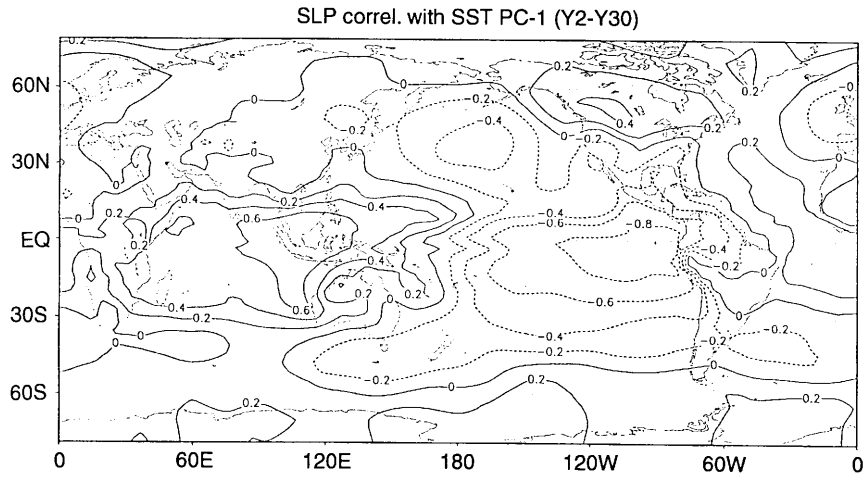

Fig. 3 Correlation of interannual sea level pressure anomalies with the time series of the first EOF of the SST. SLP data have been processed by a nine-month running mean filter

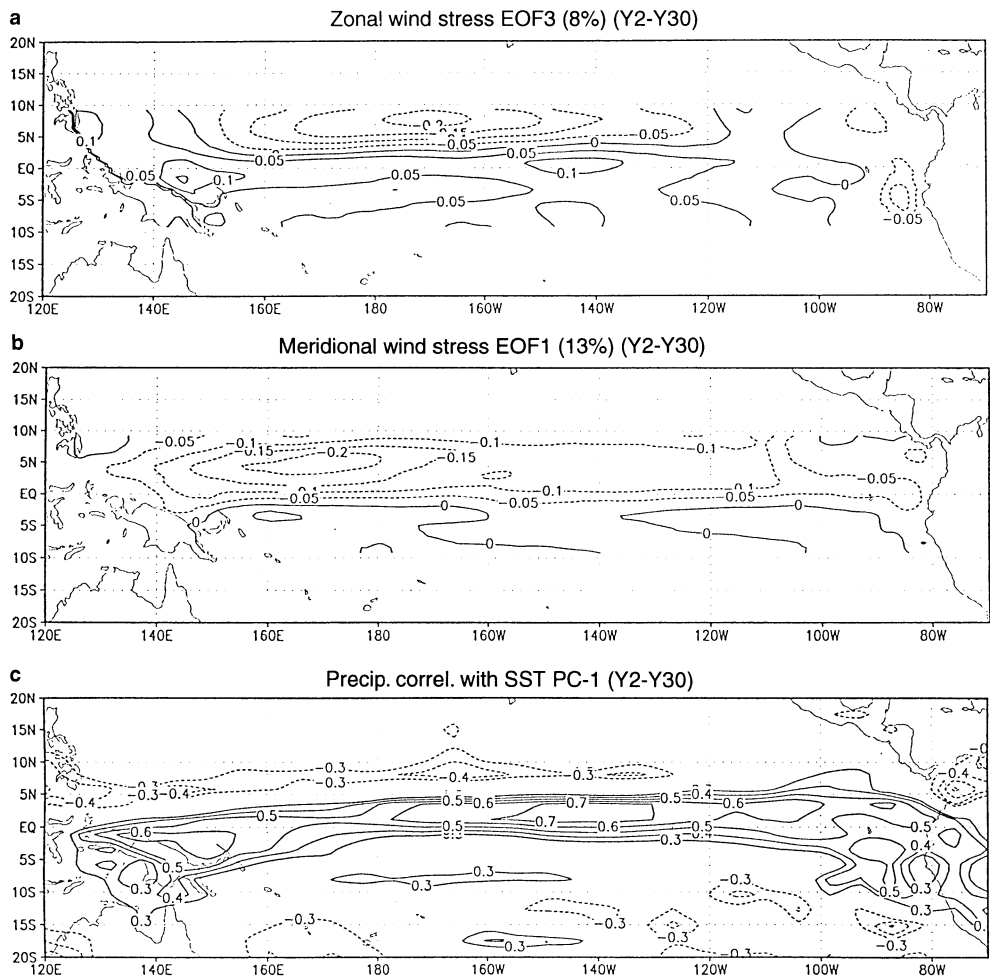

Fig. 4a–c Wind stress EOFs whose time series are best correlated to the first SST EOF time series **a** for the zonal wind stress (EOF3) and **b** for the meridional wind stress (EOF1). **c** Correlation of interannual precipitation anomalies with the time series of the first EOF of the SST. Precipitation data have been processed by a nine month running mean filter

3 Coupled evolution

To get better insight on the coupled evolution of interannual anomalies and its phasing with the seasonal cycle, we use the Extended empirical orthogonal function analysis (Weare and Nasstrom 1982) separately on SST, 20 °C isotherm depth (D20) and precipitation (P) fields, on equatorial cross sections of zonal current (EU), and on the meridional cross section of the zonal

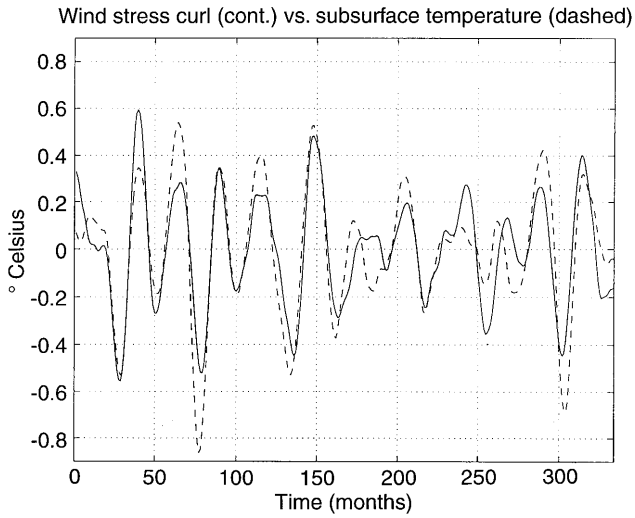

Fig. 5 Subsurface temperature fluctuations at 160 °W averaged between 3 °S–3 °N and between 70 and 210 meters at time $t + 2$ months (*dashed line*) versus the scaled difference between the wind stress curl in the Northern Hemisphere (2 °N–4 °N average) and the wind stress curl in the Southern Hemisphere (4 °S–2 °S averaged) at time t (*continuous line*). The scaling factor, computed by the least square method, equals 1.05×10^7 °C m^3 N^{-1}

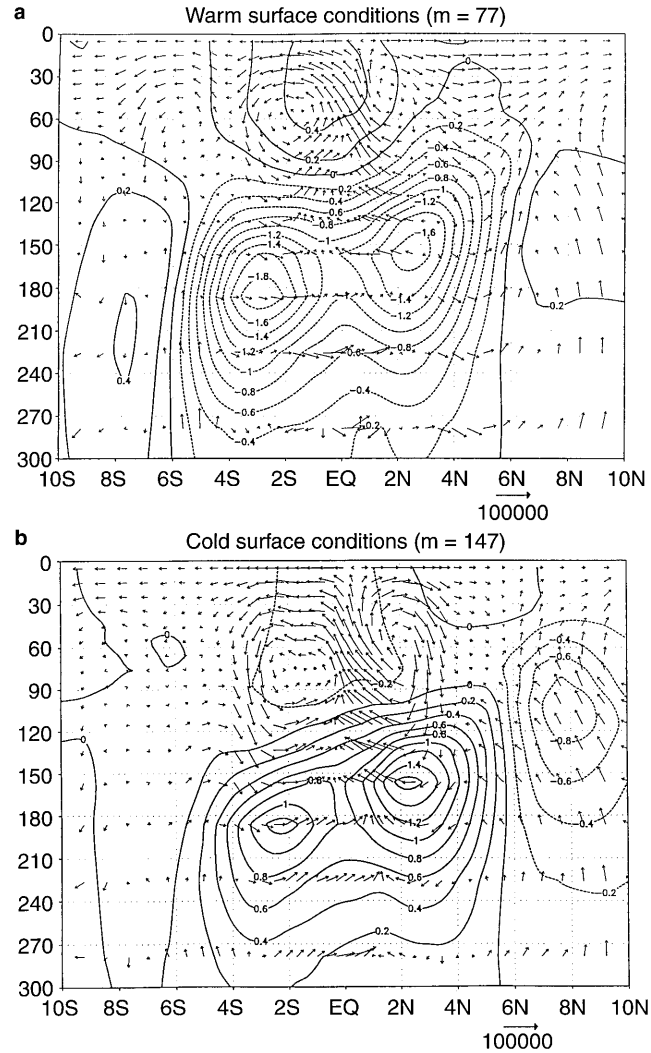

Fig. 6 **a** Mean meridional transport in m^{3}s^{-1} (*arrows*) at time t, and temperature anomalies in Celsius (*dashed lines*) on a latitude-depth plane at 160 °W at time $t + 2$ months. Here time t corresponds to the 77 month of the integration i.e., during warm surface conditions. The transport scale is indicated by the *low left arrow* in m^{3}s^{-1}. Data are filtered as indicated in the text **b** Same as **a** for $t = 147$ i.e., during cold surface conditions

current at 150 °W (MU). For computational feasibility, the dimensionality of the SST and D20 fields is reduced prior to the analysis by projecting the fields onto the first 30 EOFs, explaining 74% and 75% of total variance respectively; 60 one-month-lag windows are used. The percentages of explained variance for the two first modes that capture a quasi-biennial oscillation are 4%, 4%, 18%, 21%, 18% and 15% for SST, D20, P, ET, EU and MU respectively. For the SST and D20, explained variances are low because the EEOF method tries to capture a coherent signal from very noisy EOFs. However, the results are significant as the 2 °S–2 °N averaged reconstructed fields (not shown) are almost identical with the results presented later in Sect. 4, where 2 °S–2 °N averaged raw SST and D20 data are directly analyzed by the EEOF method. The reconstructed evolution of these fields using the first two eigenvectors that capture the quasi-biennial oscillation is presented in Figs. 7 to 12. The description starts on July of the 6th year of the integration i.e., during the end of a cold event; it ends one year later, thus covering half a biennial cycle. Reversing signs leads to the second half-cycle.

3.1 SST (Fig. 7)

At the start of the warm event, by July (0), the SST is cold in the Western Pacific (as much as 0.4 °C around 1 °S). Meanwhile, in the Central and Eastern Pacific, the sea surface temperatures are rapidly rising; in the following months, the warming intensifies and propagates westward, first along 2 °N, then along the equator. By January (+1), warm anomalies extend throughout the equatorial Pacific, with a maximum of 0.6 °C near 110 °W. Then the Eastern Pacific starts to cool, while the Western Pacific temperature still rises due to westward propagation of the anomalies: in May (+1), the maximum warming exceeds 0.4 °C and is centered on the dateline; also, from April (+1) to September (+1), it shifts to 2 °S while Eastern and Central Pacific rapidly cool.

3.2 D20 (Fig. 8)

At the onset of a warm phase, July (0), the near-equatorial thermocline (5 °S–5 °N) is deeper than normal at all

longitudes. The depth anomaly is stronger in the west, with separate maxima of about 9 m at 2 °N and 2 °S; in the east, it is maximum on the equator. To the north of the average ITCZ location (~5 °N), the thermocline is shallower than normal. In the following months, deep thermocline anomalies propagate slowly eastwards following a path centered on the equator; maximum depths of 9 m are reached between November (0) and January (+1) in the Eastern Pacific, slightly leading warm SST anomalies there. In parallel with the eastward propagation of Western Pacific deep thermocline anomalies, shallow thermocline fluctuations initially located to the north of 5 °N move equatorwards and gradually dominate the equatorial neighborhood in the Western and the Central Pacific. Then, as negative depth fluctuations arrive from the west; the Eastern Pacific equatorial thermocline begins to shallow: in May (+1) the deepening of the thermocline exceeds 3 m only to the east of 110 °W. At the end of warm surface conditions, May (+1), minima of thermocline depth in the Western Pacific are located at approximatively 2 °S and 2 °N.

3.3 Precipitation (Fig. 9)

Precipitation is of interest here as an indicator of draining; and we shall concentrate on the Western Pacific, which we expect to be dynamically active in interannual oscillations. In the Western Pacific, at the end of a cold phase: May (0), precipitation is minimum on the equator, while it is above normal to the north of 5 °N. This situation corresponds to an extreme of the weak draining phase in the Western Pacific. From then on,

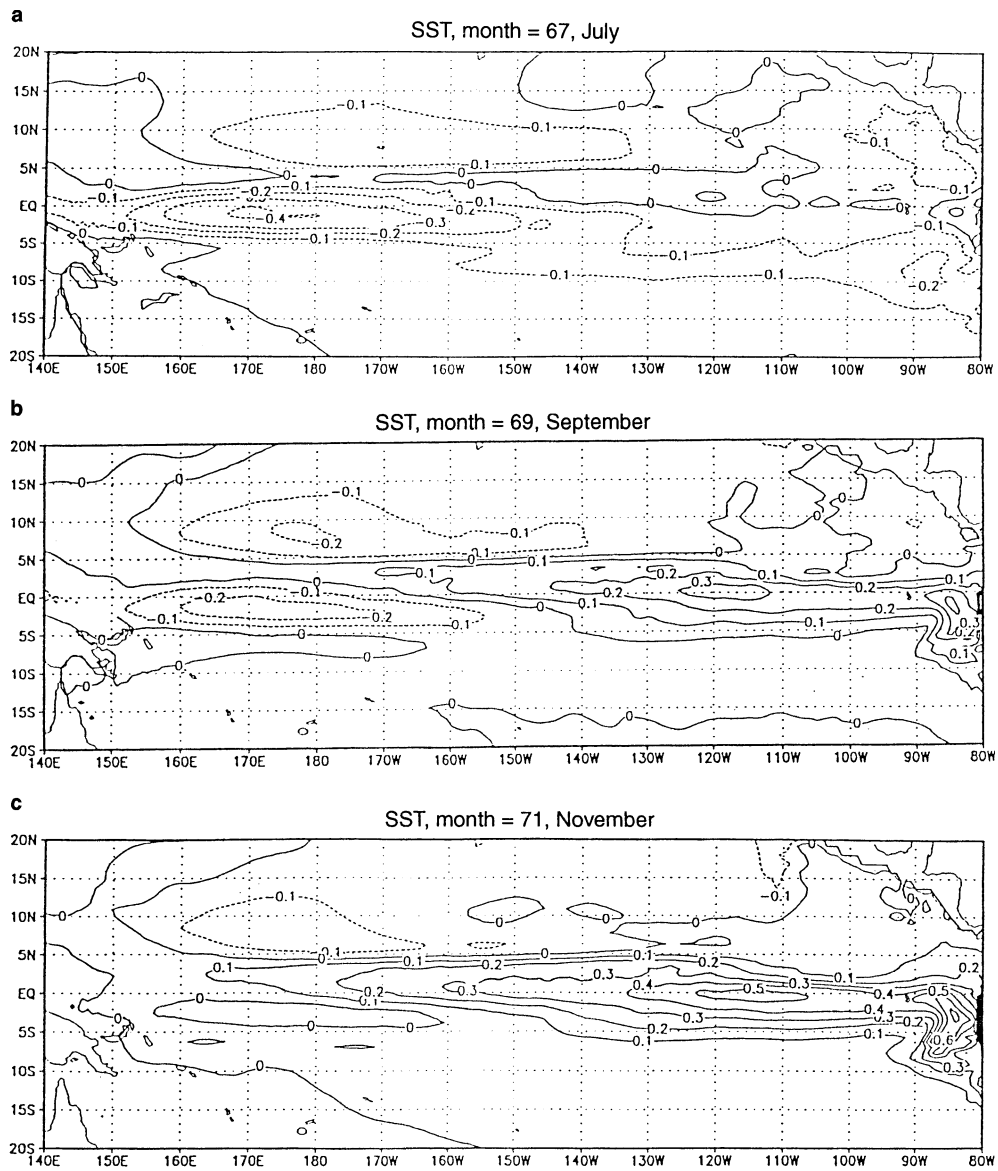

Fig. 7a–f Reconstruction of the quasi-biennial oscillation captured by the EEOF analysis for SST in °C. Half a quasi-biennial cycle is presented from July of the 6th year to May of the 7th year

Fig. 7 (*Continued*)

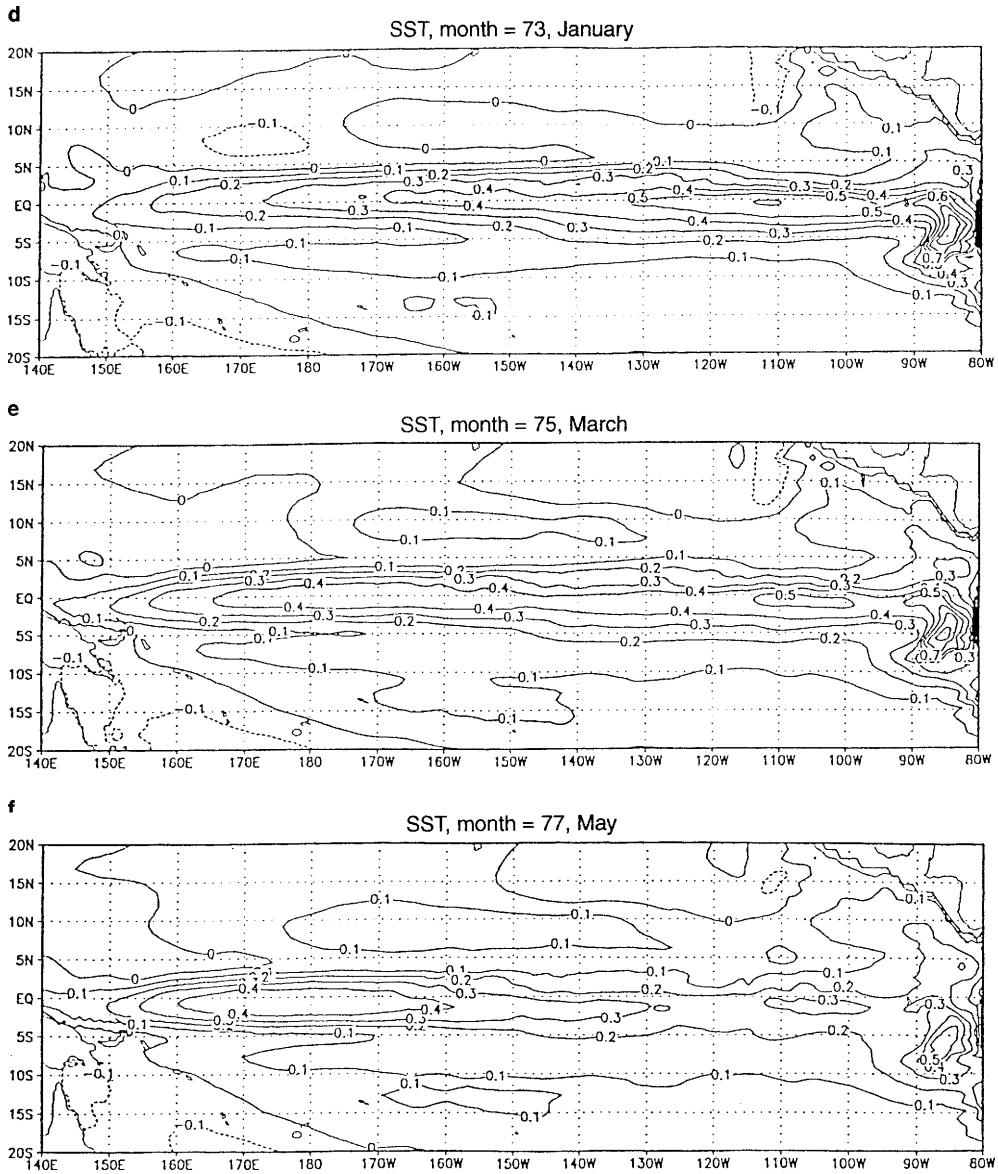

rainfall starts shifting towards the equator and draining increases; the shift from weak to strong draining in the Western Pacific occurs around November.

3.4 Equatorial temperature (Fig. 10)

Consistently with SST and D20 fluctuations, at the start of a warm episode: July (0), the ocean upper layer temperature is cold in the Western Pacific down to a depth of 90 meters, while the equatorial subsurface is warm at all longitudes. As long as weak draining keeps producing warm subsurface anomalies, i.e. until November (0), the subsurface equatorial temperature anomalies remain positive throughout the Pacific basin in spite of eastward propagation. From November (0) onwards, strong draining settles in: two months later, cold anomalies appear in the Western Pacific subsurface and start propagating eastward, progressively replacing the warm anomalies. We thus separate two successive phases related to weak, then strong Western Pacific draining in conjunction with eastward propagation: from July (0) to January (0), the thermocline deepens everywhere; from January (1) to July (1), the thermocline tilts, shallowing in the west and deepening in the east.

3.5 Zonal current along the equator (Fig. 11)

The two successive phases mentioned in 3.4 are also seen in the evolution of the zonal current anomaly field. In the first few months, the deepening of the thermocline throughout the Pacific is associated with a

lowering of the undercurrent, identified in Fig. 11 as an east-west dipole of the current anomaly with zero line along the mean thermocline depth. This dipole propagates eastwards in conjunction with the temperature anomaly, until it becomes confined in the Eastern Pacific. At that time, the Western Pacific thermocline begins to shallow under the influence of strong draining; then the undercurrent in the Western Pacific rises, which is seen in the anomaly field as the build-up of a dipole of opposite sign, which subsequently propagates eastward. Note that the upper structure of this Western Pacific dipole is much stronger than the lower one; this can be explained by the cyclonic vorticity (Fig. 12) induced by the weakening of downward Ekman pumping. However, the lower structure strengthens as it propagates eastward. Note also that the respective phasings of temperature and current anomalies are not at all reminiscent of a Kelvin wave.

3.6 Zonal current at 150 °W (Fig. 12)

In the Central Pacific as in the Western, the ITCZ is far from the equator at the beginning of the warm phase and close to the equator at the end. Thus, during a warm phase, Ekman pumping force an evolution from anticyclonic to cyclonic circulation in the upper ocean. This is clearly seen in Fig. 12. In addition, we note, in a narrow equatorial band, the strong signature of the upward motion of the EUC associated with the tilt of the thermocline during the second half of the warm phase.

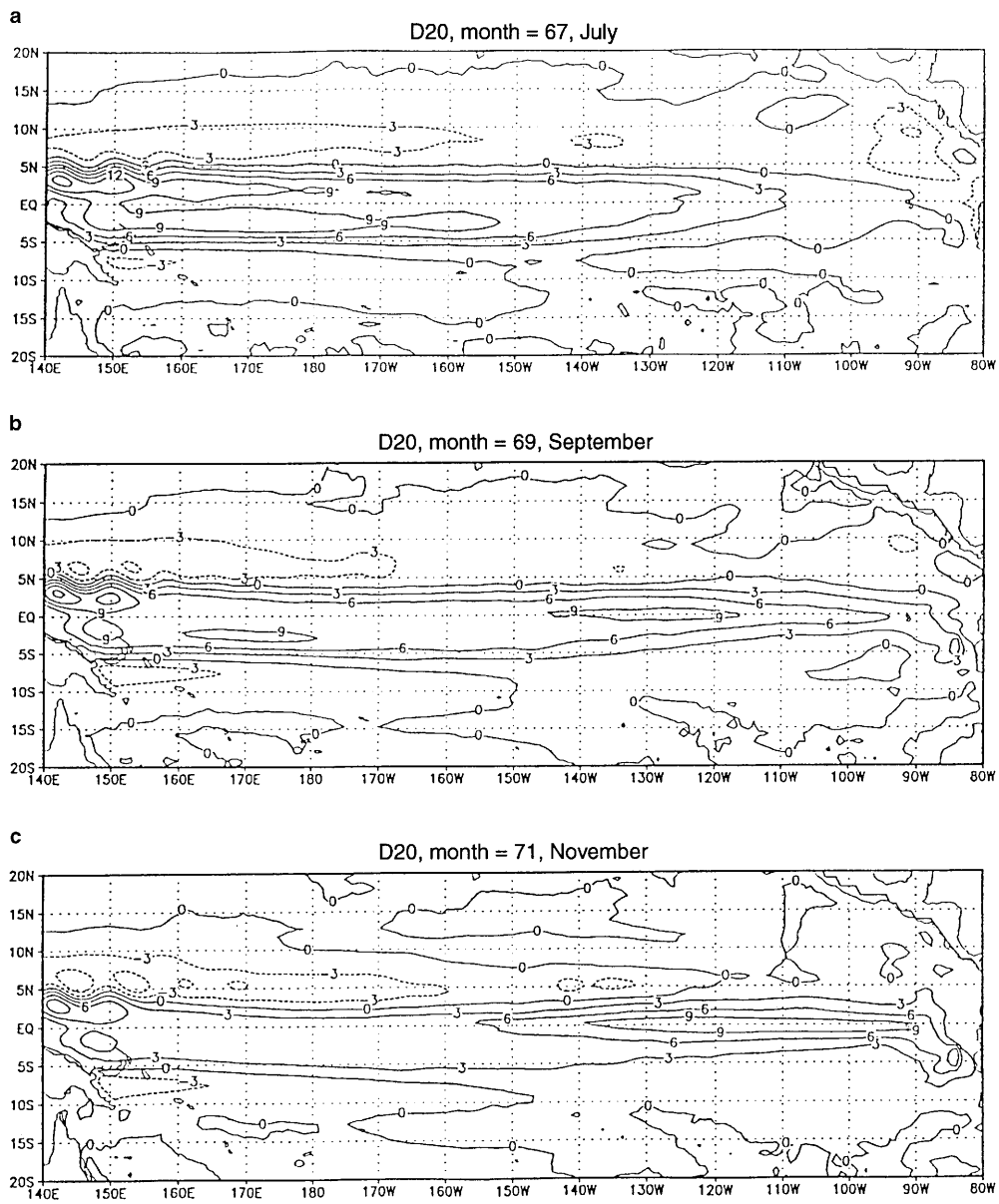

Fig. 8a–f Same as Fig. 7 but for the depth of the 20 °C isotherm in meters. *Negative values* represent a shallower D20

Fig. 8 (*Continued*)

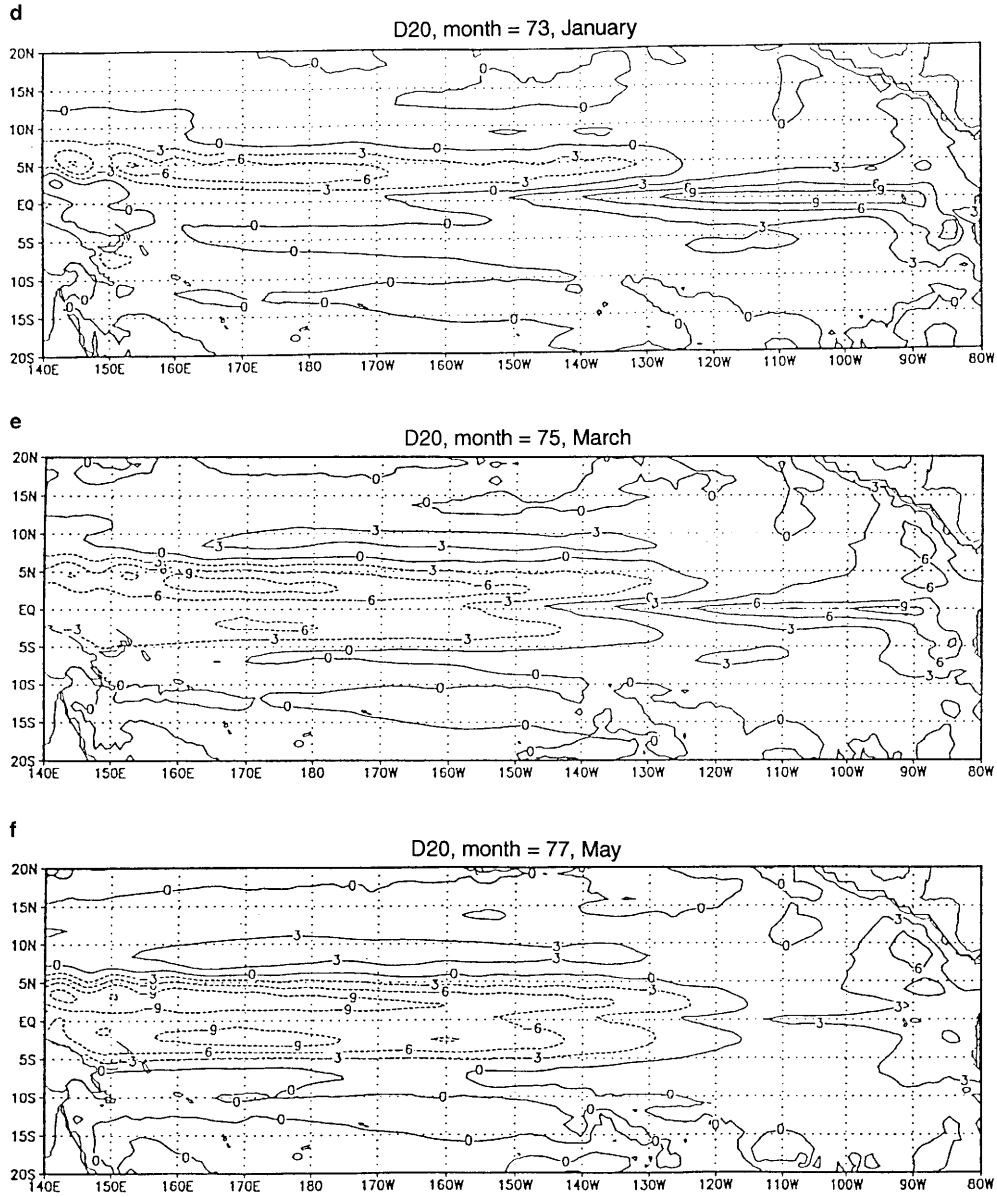

4 Seasonality of the quasi-biennial mode

We now explore the various phasings relevant to the simulated interannual variability by applying the EEOF method separately to 2 °S–2 °N averaged SST, zonal wind stress and 20 °C isotherm depth. The window used is 60 one-month-lag. The quasi-biennial mode (QB) is captured by the first pair of eigenvectors explaining respectively 26%, 7%, and 24% of total variability. The third and fourth eigenmodes capture a quasi-quadriennial oscillation but corresponds to reconstructed fields of a very weak amplitude: this mode is therefore not discussed here. It must be noted that the M-SSA analysis of observed SST data conducted by Jiang et al. (1995), indicates that the quasi-quadriennial mode dominates the real ENSO, followed by the quasi-biennial one.

The evolution of a warm phase of the QB mode between months 61 and 132 (Fig. 13) is characterized by deep thermocline anomalies (positive D20 anomalies) that appear simultaneously in the Western Pacific (140 °E to 170 °W). From 170 °W to 120 °W, D20 anomalies propagate eastwards with a velocity of about 0.4 $m\,s^{-1}$; a similar behavior is observed in the UCLA coupled model (Robertson et al. 1995). This eastward propagation is too slow to be attributed to free Kelvin waves. To the east of 120 °W, the propagation of D20 anomalies accelerates, reaching a velocity of roughly 1 $m\,s^{-1}$. As deep D20 anomalies arrive in the Eastern Pacific, the SST warms. This surface warming occurs almost simultaneously in the region between

140 °W to 80 °W, lagging the arrival of subsurface temperature anomalies by two to three months (depending on longitude). A time interval of approximately 7 mon separates maximum D20 anomalies in the Western Pacific from maximum SST anomalies in the Eastern Pacific. According to the hypothesis of Bjerknes (1969), the decrease of the zonal surface temperature gradient induced by warm SST anomalies in the Eastern Pacific is responsible for positive zonal wind stress anomalies. Our simulation support this hypothesis: positive zonal wind stress anomalies are seen to occur simultaneously with warm Eastern Pacific SST fluctuations, and are mainly located in the Western and Central Pacific (140 °E–130 °W). The same behavior characterizes the real system, as shown by a principal oscillation pattern analysis of observations (Latif et al. 1993). Positive wind stress anomalies on the equator imply a weaker atmospheric Ekman subsidence at approximatively 3 °N (see also Fig. 4a,b): stronger draining in the Western and Central Pacific then yields cold subsurface anomalies. Maximum values of these subsurface temperature anomalies are reached six to seven months after the occurrence of maximum SST deviations in the Eastern Pacific.

As in our model as in observations and in many previous simulations, free Kelvin waves cannot explain the slow eastward propagation of subsurface temperature anomalies, we have to find another mechanism that may carry heat content fluctuations from the Western to Eastern Pacific in a time scale of five to six months. We have performed Lagrangian experiments where sets of particles released from thermocline level in either the Western or the Central Pacific are advected by the mean currents; the simulations (not shown)

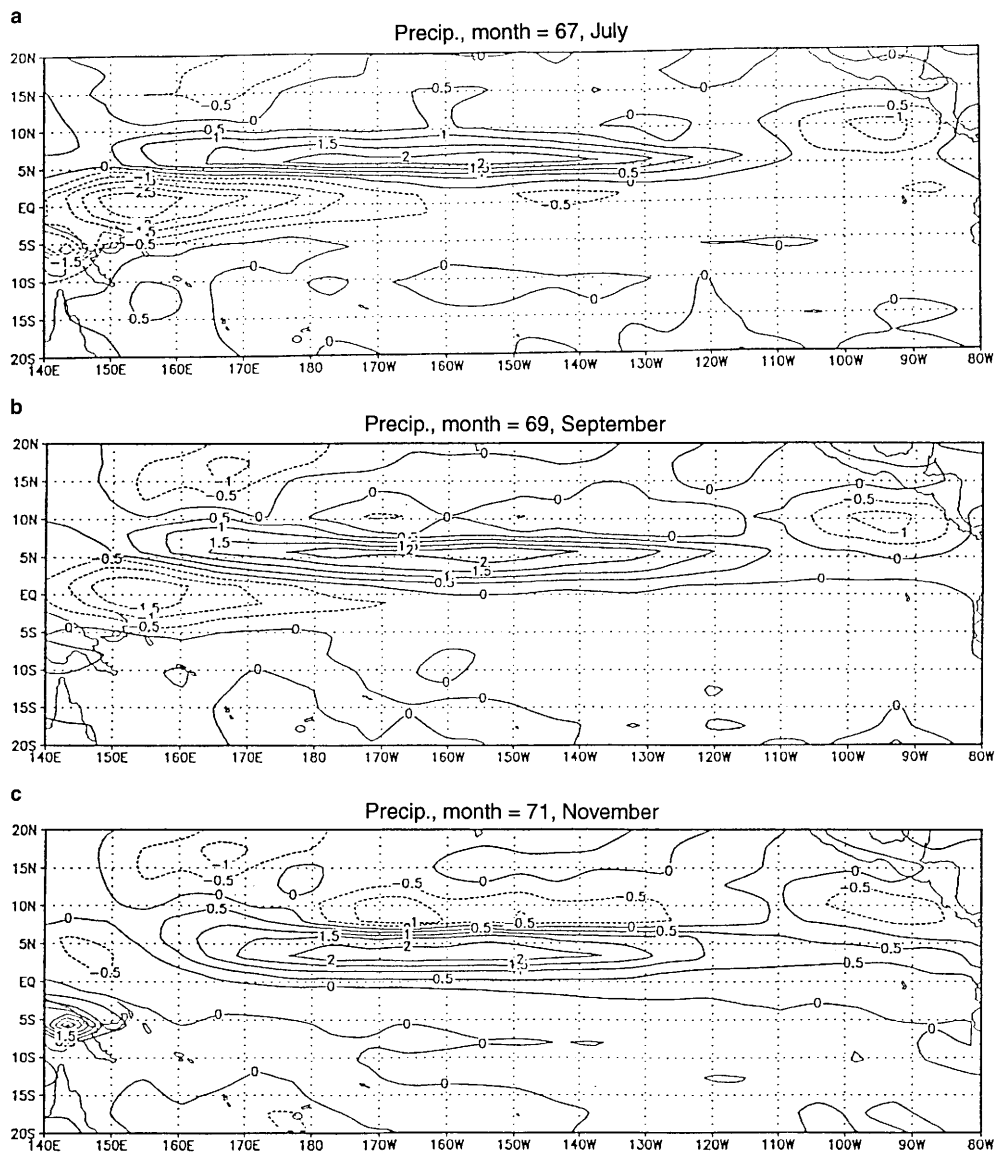

Fig. 9a–f Same as Fig. 7 but for precipitation in mm/day

Fig. 9 (*Continued*)

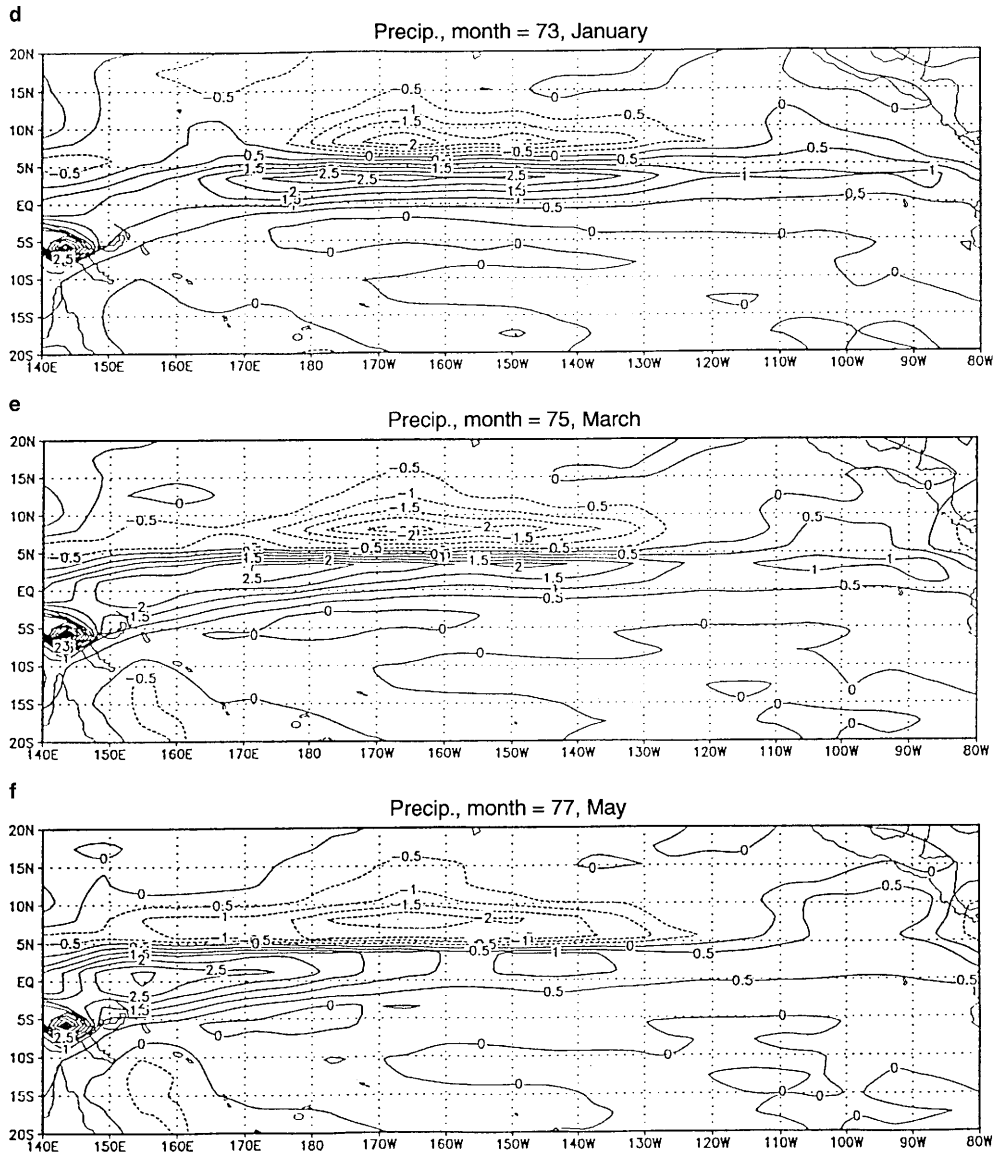

suggest that advection (zonal, vertical and meridional) is a plausible candidate for setting the necessary time scales in our model.

A second question concerns the seasonality of the simulated (and observed) interannual variability. In Part I we have shown that meridional draining, which is responsible for poleward "dissipation" of subsurface signals, varies seasonally. Figure 14 describes the simulated unfiltered meridional transport divergence, integrated from 5 °S to 5 °N and between 160 °E and 90 °W in the upper 55 meters of the ocean model. During the boreal spring almost 60 Sverdrups of water leave the equatorial neighborhood, six times more than in autumn. It clearly follows that, for producing similar effects in the Eastern Pacific, Western Pacific subsurface temperature anomalies occurring in late winter and early spring should be six times larger than in summer and early autumn. Therefore, draining acts as a seasonal dam which synchronizes interannual behavior with the annual cycle.

5 Summary and conclusion

The analysis of the behavior of the LMD-LODYC tropical Pacific-global atmosphere model suggests a new mechanism to tentatively account for interannual oscillations in the tropical Pacific. In this mechanism, the phase inversion between cold and warm surface conditions is driven by the coupling between the meridional motion of organized convection and the three-dimensional circulation of the upper ocean. During warm interannual events, the SST in the Eastern and Central Equatorial Pacific is warm. As expected

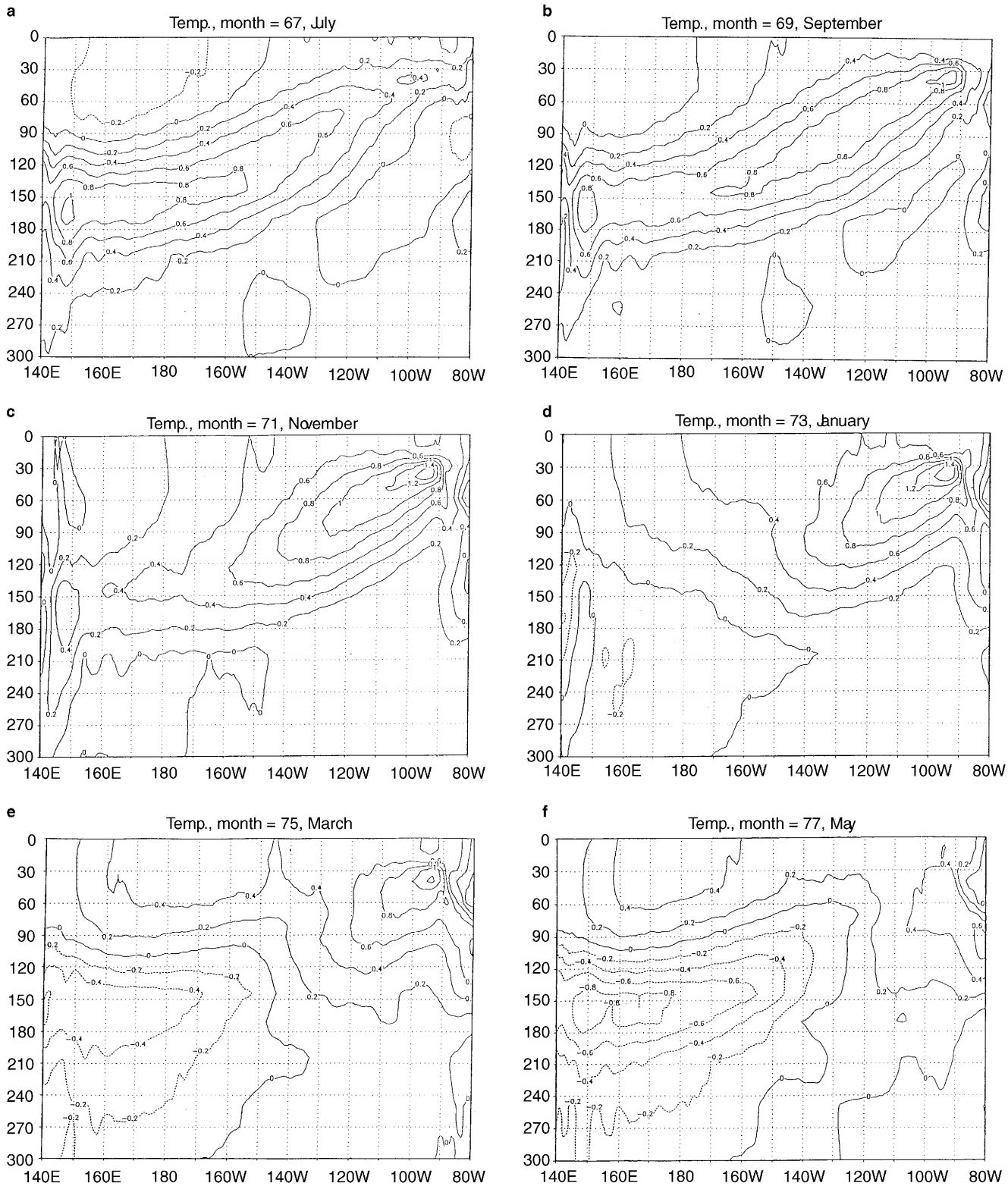

Fig. 10a–f Same as Fig. 7 but for ocean temperature along a longitude, depth equatorial section in °C

from the Bjerknes (1969) hypothesis this warming weakens the zonal wind stress in the Western and Central Equatorial Pacific. Accordingly, the meridional gradient of the zonal wind stress to the north of the equator decreases and therefore Ekman subsidence between the equator and the mean location of the ITCZ weakens. Additionally, warm SST anomalies propagate westward and warm the Western Pacific

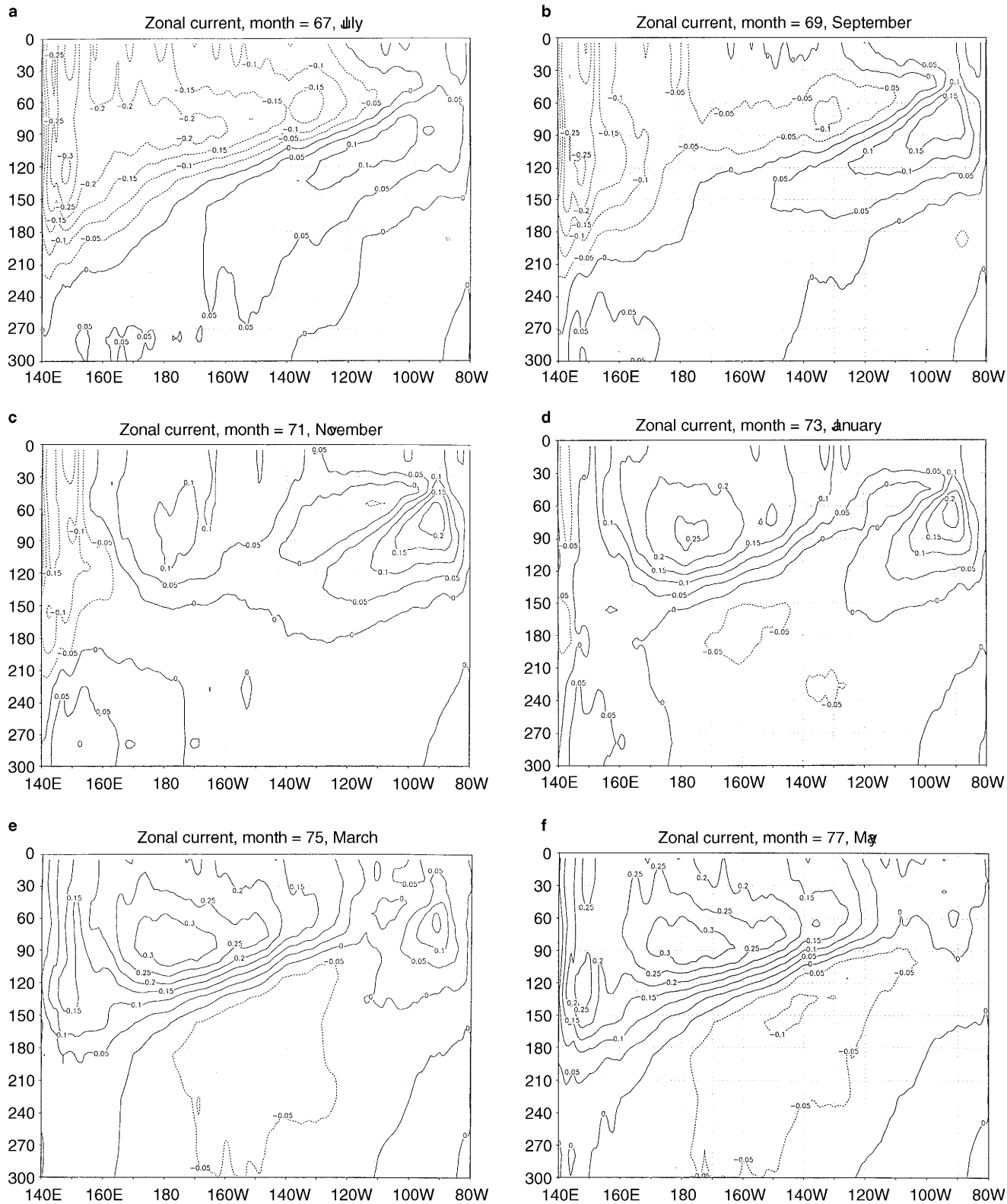

Fig. 11a–f Same as Fig. 7 but for zonal current along a longitude – depth equatorial section in ms^{-1}

surface. A weaker meridional SST gradient to the north of the equator in conjunction with warm SSTs result in an equatorward shift of the ITCZ; this equatorward shift is consistent with the decrease of Ekman subsidence close to the equator, and leads to strong poleward draining of near surface equatorial waters. It is this strong draining which then explains the cooling of the ocean subsurface, with maximum values at the Ekman

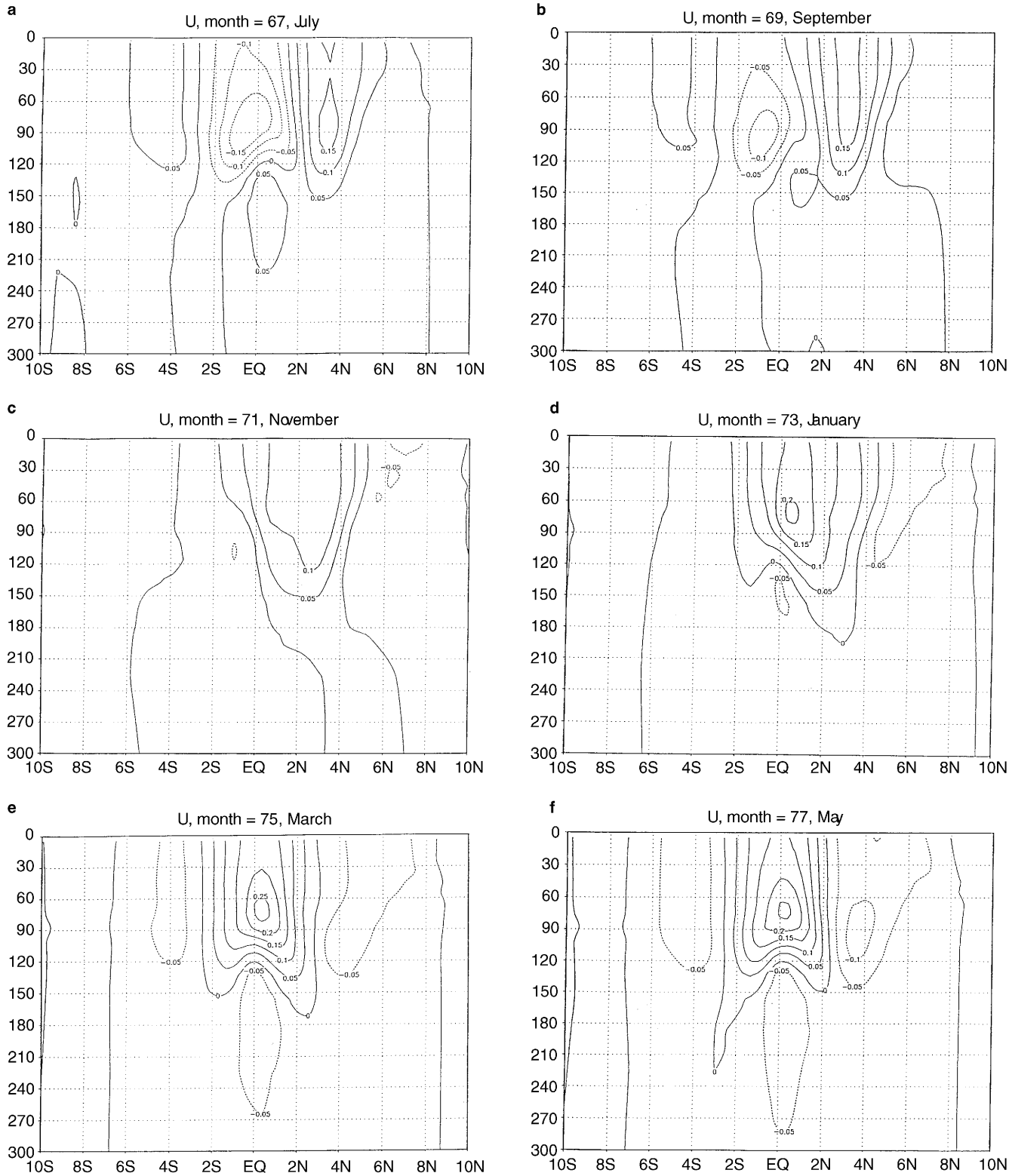

Fig. 12a–f Same as Fig. 7 but zonal current along a latitude – depth section at 150 °W in ms^{-1}

cell subsidence latitude, about 3 ° from the equator. Cold temperature anomalies are then advected eastward by the mean EUC. Seven months later, Western Pacific cold subsurface anomalies affect the near surface layers in the Central Pacific. Cold SSTs in the Central and Eastern Pacific increase the zonal SST gradient and thus the equatorial zonal stress in the Western and Central Pacific. The corresponding weak

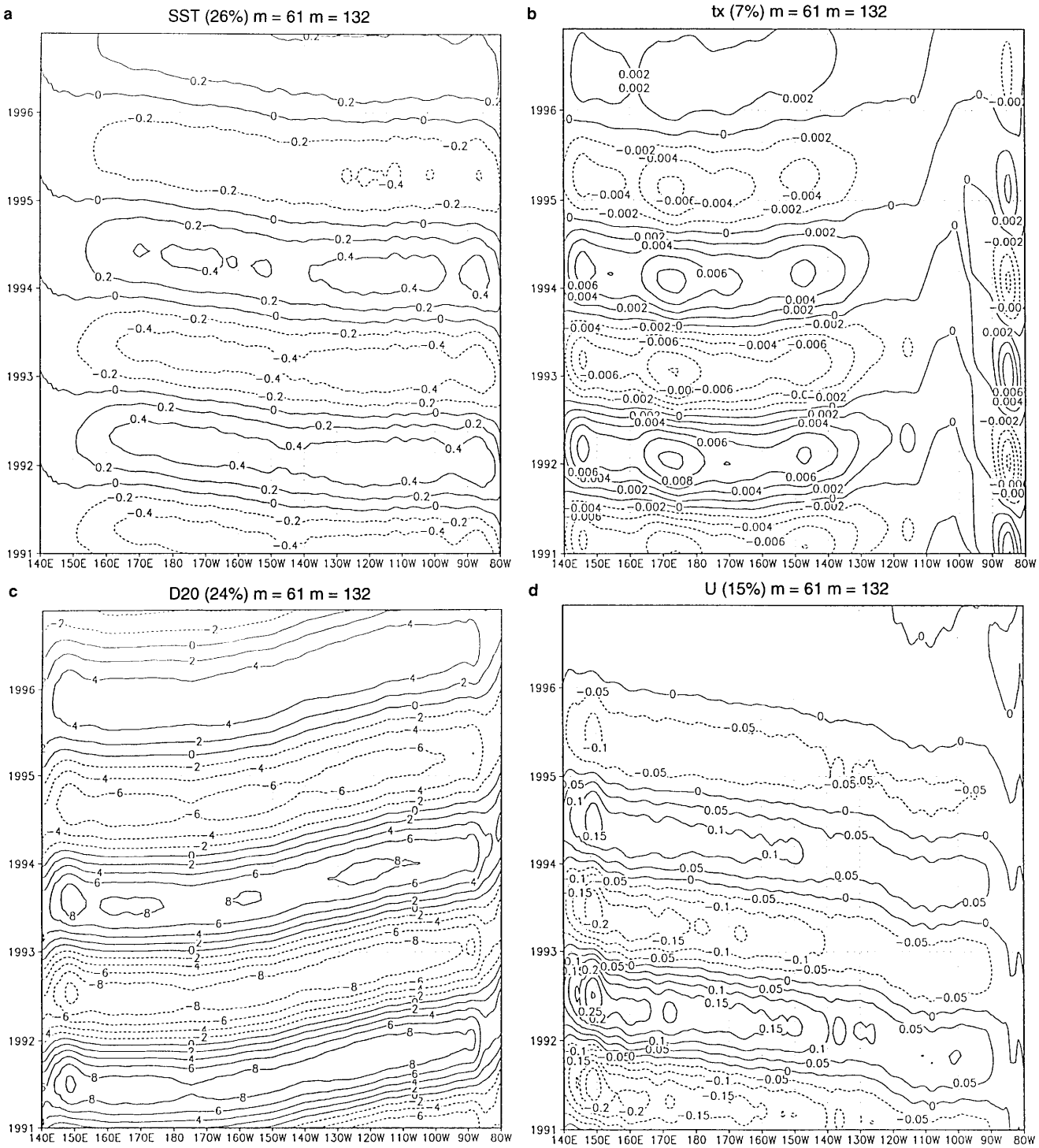

Fig. 13a–d Reconstructed quasi-biennial oscillation obtained by the EEOF analysis of equatorial data. **a** SST in °C, **b** zonal wind stress in Nm^{-2}, **c** depth of the 20 °C isotherm in m (*negative values* correspond to shallowing), and **d** zonal current in ms^{-1}

draining warms the equatorial subsurface and thus set the seeds for the next warm surface event.

It is during boreal summer and autumn that subsurface temperature anomalies in the Central and Eastern Pacific are more likely to remain trapped in the vicinity of the equator, due to the seasonal background of weak meridional draining. During boreal spring, a very significant fraction, four times more than in autumn, of anomalously warm or cold water parcels would be drained out of the equatorial band instead of

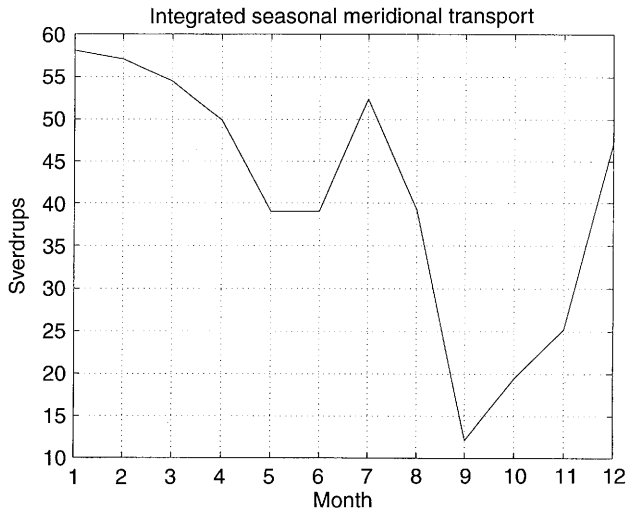

Fig. 14 Mean annual meridional transport integrated between 5 °S–5 °N and 160 °W–90 °W in Sverdrups

propagating eastward after being recycled by near-equatorial overturning.

At first glance, in contrast with the delayed oscillator mechanism, wave reflection at eastern or western boundaries is not required. Boundaries are important only through their effect on the mean state of the coupled system, and for selecting the oscillation time scales through the width of the basin. An important piece in the mechanism proposed here is the slow eastward advection of subsurface temperature anomalies. The eastward propagation of the subsurface temperature fluctuations present some resemblance with the subsurface behavior in the conceptual model of Jin (1997), where heat content departures in the Western Pacific are responsible for the rate of change of heat content anomalies in the Eastern Pacific.

Another important aspect of our proposed mechanism is that it is open to effects from extra-Pacific sources of variability. Indeed, the tropical Pacific ITCZ cannot be viewed in isolation from the atmospheric circulation in other tropical regions. The coupling between the ITCZ and the upper ocean circulation is expected to induce teleconnections with other tropical basins, especially the nearby Indian Ocean. A correlation between the intensity of the Asian monsoon and zonal winds on the Western Equatorial Pacific has been noticed by Webster and Yang (1992).

The above considerations imply a number of prerequisites for a realistic modelling of the interannual variability of the Tropical Pacific. The relation between surface conditions and convection must be as realistic as possible. On the ocean side, structures like the mean Equatorial Under Current which advects subsurface water parcels eastwards, and the meridional recirculation cells must be correctly represented; meridional discretizations of at least 0.5 ° in latitude should be used. As for the interface between the ocean and the atmosphere, it is clear that equatorial scales of the order of 3 ° in latitude must not be damped. It is therefore suggested that either a very dense atmospheric discretization or a delocalized physics scheme should be used.

The ENSO mechanism we propose here is based on a 30 y simulation by the global atmospheric general circulation model of the LMD interfaced through the delocalized physics method with the Tropical Pacific Ocean general circulation model of the LODYC. Like many others, this coupled model suffers from systematic biases: an excessively warm SST near the Ecuador coast associated with unrealistic local westerlies; an unrealistically narrow equatorial cold tongue extending too far into the Western Pacific warm pool. And though the ENSO behavior of the model is clearly identified, its amplitude is only about half that observed, with a dominant period of two years instead of four. Our contention here is that these biases, although they surely influence quantitative features of the coupling processes (like time scales in connection with the strength of the undercurrent), should not significantly affect the principle of the proposed mechanisms. In fact, these mechanisms even bring some consistency to the model biases. For example, the too short time scale of our modelled ENSO is consistent with our too strong mean longitudinal slope of the thermocline in the West Pacific (see Part I), and with our underestimation of the amplitude of El Niño, which goes along with an overestimation of the mean slope of the thermocline in the Central Pacific. Both biases tend to speed up the advection of subsurface temperature anomalies by the mean Equatorial Undercurrent, leading to an underestimation of the ENSO time scale.

Acknowledgements This work has been supported by the European Union under contracts EV5V-CT92-0121 and ENV4-CT95-0109, and the PNEDC (Programme National d'Étude de la Dynamique du Climat). The numerical experiments have been conducted at IDRIS (Institute de Développement et de Recherches en Informatique Scientifique) of the Centre National de la Recherche Scientifique. Comments by two anonymous referees have helped to improve the text.

References

Bjerknes J (1969) Atmospheric teleconnections from the equatorial Pacific. Mon Weather Rev 97 : 163–172

Battisti DS, Hirst AC (1989) Interannual variability in the tropical atmosphere-ocean system: influence of the basic state, ocean geometry, and nonlinearity. J Atmos Sci 46 : 1687–1712

Cane MA, Zebiak SE (1985) A theory for El Niño and the Southern Oscillation. Science 228 : 1084–1087

Hirst AC (1986) Unstable and damped equatorial modes in simple coupled ocean-atmosphere models. J Atmos Sci 43 : 606–630

Jiang N, Neelin JD, Ghil M (1995) Quasi-quadriennial and quasi-biennial variability in the equatorial Pacific. Clim Dyn 12 : 101–112

Jin F-F (1996) Tropical ocean-atmosphere interaction, the Pacific cold tongue, and the El Niño-Southern Oscillation. Science 274 : 76–78

Jin F-F (1997) An Equatorial ocean recharge paradigm for ENSO. Part I: conceptual Model. J Atmos Sci 54 : 811–829

Jin F-F, Neelin JD (1993a) Modes of interannual tropical ocean-atmosphere interaction – a unified view. Part I: numerical results. J Atmos Sci 50 : 3477–3502

Jin F-F, Neelin JD (1993b) Modes of interannual tropical ocean-atmosphere interaction – a unified view. Part III: analytical results in fully coupled cases. J Atmos Sci 50 : 3523–3540

Latif M, Sterl A, Maier-Reimer E, Junge MM (1993) Structure and predictability of the El Niño/Southern Oscillation phenomenon in a coupled ocean – atmospheric general circulation model. J Clim 6 : 700–708

Lau K-M (1981) Oscillations in a simple equatorial climate system. J Atmos Sci, 38 : 248–261

Lau N-C, Philander SGH, Nath MJ (1992) Simulation of ENSO-like phenomena with a low resolution coupled GCM of the global ocean and atmosphere. J Clim 5 : 284–307

Murakami M (1979) Large-scale aspects of deep convective activity over the GATE area. Mon Weather Rev 107 : 994–1013

Neelin JD (1991) The slow sea surface temperature mode and the fast-wave limit: analytic theory for tropical interannual oscillations and experiments in a hybrid coupled model. J Atmos Sci 48 : 584–606

Neelin JD, Jin F-F (1993) Modes of interannual tropical ocean-atmosphere interaction – a united view. Part II: analytical results in the weak-coupling limit. J Atmos Sci 50 : 3504–3522

Philander SGH, Pacanowski RC, Lau N-C, Nath MJ (1992) Simulation of ENSO with a global atmospheric GCM coupled to a high-resolution, tropical Pacific Ocean GCM. J Clim 5 : 308–329

Rasmusson EM, Carpenter TH (1982) Variations in tropical sea surface temperature and surface wind fields associated with the Southern Oscillation/El Niño. Mon Weather Rev 110 : 354–384

Robertson AW, Ma C-C, Ghil M, Mechoso CR (1995) Simulation of the Tropical Pacific climate with a coupled ocean-atmosphere general circulation model. Part II: interannual variability. J Clim 8 : 1199–1216

Suarez MJ, Schopf PS (1988) A delayed oscillator for ENSO. J Atmos Sci 45 : 3283–3287

Trenberth KE, Shea DJ (1987) On the evolution of the Southern Oscillation. Mon Weather Rev 115 : 3078–3096

Vintzileos A, Delecluse P, Sadourny R (1997) On the mechanisms in a tropical ocean–global atmosphere coupled general circulation model. Part I: mean state and the seasonal cycle. Clim Dyn 15 : 43–62

Wallisez DE, Gautiez C (1993) A satellited–derived climatology of the ITCZ. J Clim 6 : 2162–2174

Weare BC, Nasstrom JS (1982) Examples of extended empirical orthogonal function analyses. Mon Weather Rev 110 : 481–485

Webster PJ, Yang S (1992) Monsoon and ENSO: selectively interactive systems. Q J R Meteorol Soc 118 : 877–927

Wyrtki K (1985) Water displacements in the Pacific and the genesis of El Niño cycles. J Geophys Res 90 : 7129–7132

Zebiak SE, Cane MA (1987) A model El Niño Southern Oscillation. Mon Weather Rev 115 : 2262–2278

Zhang R, Levitus S (1996) Structure and evolution of interannual variability of the tropical Pacific under ocean temperature. J Geophys Res 101 : 20 501–20 524